Chapter 1 *Introduction and Literature Review*

1.1 Introduction

Energy harvesting from renewable energy sources is the main objective of the researchers in this time of energy scarcity. Adjacently, researchers are also working on developing new ways to store this energy in the form of electricity using batteries, fuel cell, supercapacitors etc. Among all, supercapacitors are one of the best device for energy storage, serve as a channel between traditional capacitors and batteries. They have number of advantages over batteries and traditional capacitors, such as high power and energy density, long lifetime, fast charging and discharging, easy maintenance and most importantly, no environmental pollution. In this context, over the last few decades, there has been a gradual increase in scientific interest to use of various nanostructured engineering materials for supercapacitors and other applications. These nanostructured materials outperform their bulk counterparts in terms of their chemical kinetics, chemical stability, shorter ionic diffusion path lengths, high surface area, and abundance of active sites for electrochemical reactions. The properties of nanoparticles are strongly influenced by the factors like morphology, crystallinity, crystallographic structure and density [11]. Specifically, transition metal oxides (TMOs) are one of the most intriguing classes of nanostructured materials, with a diverse range of crystal structures, high chemical activity, low production costs and are universally recognized as the foundation of next-generation advanced devices. The

multiple valance states with partially filled outer-d orbitals of TMOs evoke interesting chemical and physical properties which build the interest of researchers to discover their structure property correlation. These are the compounds which form a metal-oxygen bond of various types whose nature varies from ionic to covalent to metallic. For example, while oxides like RuO_2 [12], $LaNiO_3$ [13] show metallic properties, oxides like $BaTiO_3$ [14], MnO_3 [15] exhibit highly insulating behaviour. Furthermore, some TMOs, such as TiO_2, SnO_2 , and MnO_2, are semiconductors [16]–[18].

Among these nanostructured TMOs, Manganese dioxide (MnO_2) nanoparticles (NPs) are one of the most interested functional metal oxide, getting attention among researchers because of its economic, nontoxicity, environmentally friendly nature and abundance in comparison to other oxides. It is a dark brown-colored material that occurs naturally as the mineral pyrolusite. MnO_2 NPs are easy to prepare and have good stability due to which it has been applied in various applications such as it is widely used as a catalyst [19], toxic metal absorbent [20], octahedral molecular sieves [21], sensors [22], photocatalysts [23], microbial fuel cells [24], electrodes for Li batteries [25], Na batteries [26], Mg batteries [27] and supercapacitors [28][29]. MnO_2 nanomaterials have large specific surface area and surface defects, implying greater activity and novel properties. These properties can be tuned by varying the synthesis techniques.

1.1.1 Crystal Structure

The basic framework of MnO_2 crystallographic structure is made up of MnO_6 octahedra, known as octahedral molecular sieves (OMSs) [30]. These OMSs are linked in different ways by sharing their edges and vertices (figure 1.1), resulting in the formation of one-dimensional (1D), two-dimensional (2D) and three-dimensional (3D) crystallographic

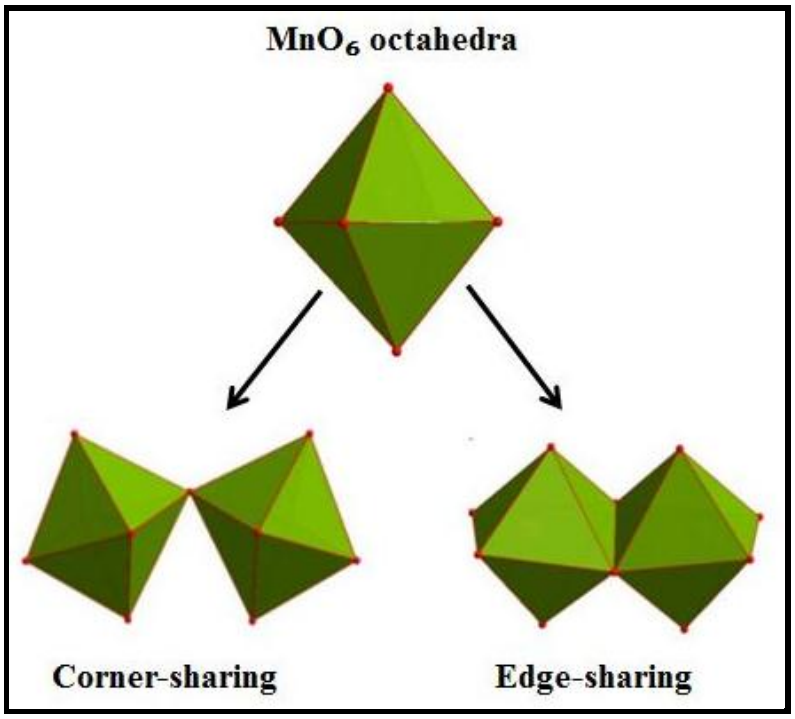

Figure 1.1: *MnO_6 octahedral molecular sieve (OMS) and its sharing pattern.*

configurations. 1D tunnel structures consists of α, β and γ-MnO_2 [31]. 2D and 3D groups are composed of layer structured δ-MnO_2 and spinel structured λ-MnO_2, respectively. α-, β-, γ-, δ- and λ-MnO_2 are formed by interlinking of MnO_6 octahedra, which have tunnels or interlayer gaps of varying magnitude (n x m), as shown in figure 1.2. α-MnO_2 is made up of two MnO_6 octahedral chains that are connected at the corners and sharing there edges to formulate (1x1) and (2x2) tunnels that runs along the third axis of tetragonal unit cell (figure 1.2a) [32]. The tunnels formed in α-MnO_2 are of diameter ~4.6 Å, which is appropriate for the intercalation/deintercalation of alkali cations like Li, Na, K, Ba, H_3O or water molecules [33]. A series of MnO_6 octahedral units share their edges results in the formation of 1D (1x1) tunnel structure pyrolusite, β-MnO_2 of size 1.89 Å (Figure 1.2b) [34]. Because of its narrow size, it cannot accommodate cations. Thermodynamically, β-MnO_2 possesses the most stable structure among all polymorphs of MnO_2. The

uncontrolled growth of ramsdellite, R-MnO_2, (1x2) and pyrolusite, β-MnO_2, (1x1) domains leads to the formation of γ-MnO_2 (figure 1.2c) [35]. 2D layers of edge shared MnO_6 octahedra form birnessite, δ-MnO_2 with an interlayer spacing of ~7 Å (figure 1.2d) [36]. MnO_2 sheets can be stabilized by inserting adequate number of water (H_2O) molecules or cations like Na^+ or Li^+ between them. λ-MnO_2 is a usual spinel structure of 3D (1 x 1) tunnels that significantly promotes the transfer of electrons [37]. As a result, it has been widely utilized as an electrode material in electrocatalysis. The structures with various types of tunnels formed as well as their size are illustrated schematically in figure 1.2 and Table 1.1.

Table 1.1: Crystallographic data of polymorphs of MnO_2.

Compound	**Structure, space group**	**Lattice parameters (a, b, c) Å**	**Tunnel structure**
α- MnO_2	Tetragonal, I4/m	9.818 ,9.818, 2.859	(2 x 2) tunnel
β- MnO_2	Tetragonal, $P4_2/mnm$	4.398, 4.399, 2.861	(1 x 1) tunnel
R- MnO_2	Orthorhombic, Pbnm	4.53, 9.27, 2.87	(1 x 2) tunnel
γ- MnO_2	Complex tunnel (hexagonal)		(1 x 1)/(1 x 2) tunnel
δ- MnO_2	Monoclinic, $P6_3/mnm$	2.918, 2.931, 7.432	(1 x ∞) layer
λ- MnO_2	Cubic spinel, Fd3m	8.040, 8.040, 8.040	(1 x 1) tunnel

The properties of MnO_2 are essentially determined by its crystallographic structure. The exceptional structure flexibility of MnO_2 is appealing because it allows for the creation of

variety of structures, making it a practical tool for studying the effects of dimensionality and crystallographic framework on catalytic, electrochemical, and magnetic properties.

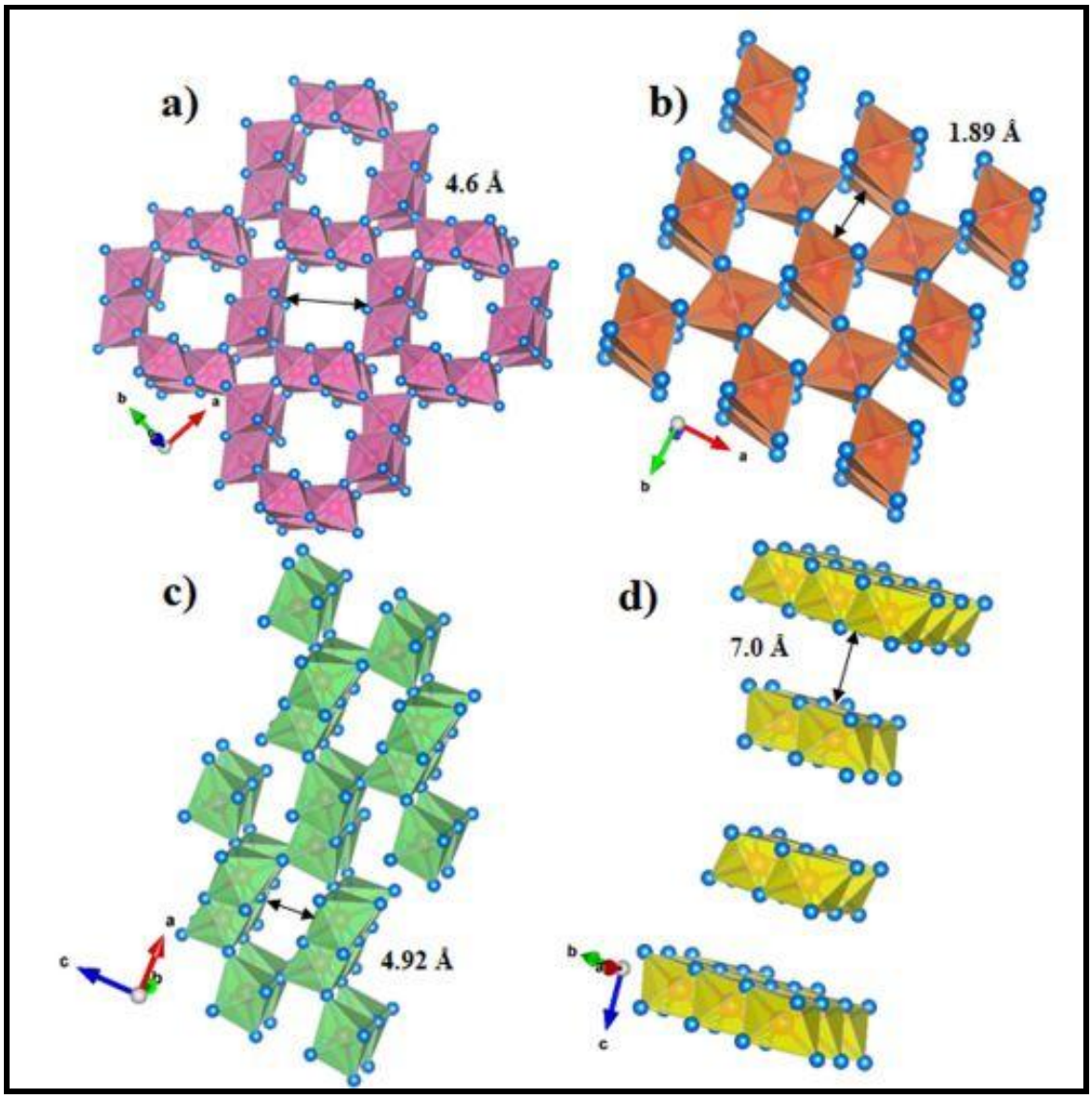

Figure 1.2: *Arrangement of various MnO_2 framework by forming tunnel (n x m) structures [38].*

Since the capacitance is generated by the insertion or deinsertion of ions or electron/proton in the tunnels of MnO_2, only those crystallographic structures which have enough space to admit these cations are anticipated to be useful for investigations related to its capacitive performance. The significant number of cations or protons inserted/exiled into/from the MnO_2 framework, and thus its capacitive performance is expected to be largely determined by either from tunnel size or interlayer saperation of the layers of MnO_6 octahedral sheets [31]. Structural parameters of all the polymorphs of MnO_2 are illustrated in table 1.1.

1.1.2 Magnetic Behaviour

Previously, the majority of MnO_2 research focused on the investigation of electrochemical properties. MnO_2 in bulk is antiferromagnetic [38]. When the size is reduced to the nanometer range, unconventional and intriguing magnetic properties in nanostructured MnO_2 can appear that are completely different from the bulk counterpart. As previously stated that MnO_2 has a high degree of structural flexibility and can exists in a variety of crystallographic forms, influences its physical and chemical properties. The most stable polymorph of MnO_2 is β-phase, while α, γ, δ, and λ are metastable states. These metastable compounds acquire an external cation to stabilize their structure, which causes structural changes [33][39]. The complicated magnetic characteristics of MnO_2 are extremely intriguing to study because of their unusual different ordered magnetic phases, which are most likely caused by frustrated magnetic structures and the existence of a significant amount of cations in the tunnels. The presence of different Mn^{+4} and Mn^{+3} concentrations is also responsible for the variation in magnetic properties of nanostructured MnO_2 [40]. To comprehend the complex magnetic behaviour of MnO_2, it is necessary to investigate magnetism and possible interactions between the cations present in the compound. The

phenomenon of mixed-valence occurs in many transition metal oxides, where the metal is present in more than one oxidation state. The rate of electron transfer between different oxidation states determines the properties of such compounds [41][42]. The nanostructured transition metal oxides such as MnO, MnO_2, FeO, NiO, and CoO exhibit a magnetic phase transition from paramagnetic to antiferromagnetic upon cooling [43]–[45]. They can also exhibit ferromagnetism or spin-glass behaviour in some cases.

Ferromagnetism

Ferromagnetic materials are the materials that possess spontaneous magnetization even though no external magnetic field is present. When a weak external magnetic field is applied, they get strongly magnetized. According to Weiss theory, ferromagnets in a demagnetized state consist of numerous tiny areas known as domains which are spontaneously magnetized. The direction of magnetization of these domains is in such a way that there is no net magnetization. After applying external field, each domain sets magnetized in the direction of field and the magnetic moments are saturated along magnetic field direction. The process of magnetization is demonstrated in figure 1.3. During the entire process, the magnitude of magnetization of domains remain same only the direction changes. Cobalt, iron, nickel, and metals are some of the most frequent examples of these materials. Ferromagnetism exists only below the Curie temperature, T_c above which the material becomes paramagnetic and its susceptibility then obeys Curie-Weiss law-

$$\chi = C/(T - T_c) \qquad [1.1]$$

Figure 1.4 shows the susceptibility-temperature dependence of a ferromagnetic material. At $T > T_C$ the χ is positive and when T becomes equal to T_C, χ is infinite, which correlated with the order spontaneous phase [46].

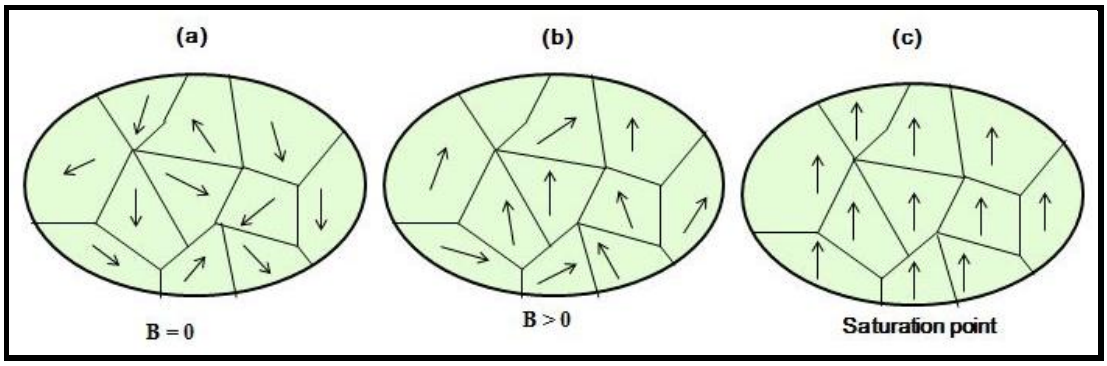

Figure 1.3: *The magnetization process in ferromagnets.*

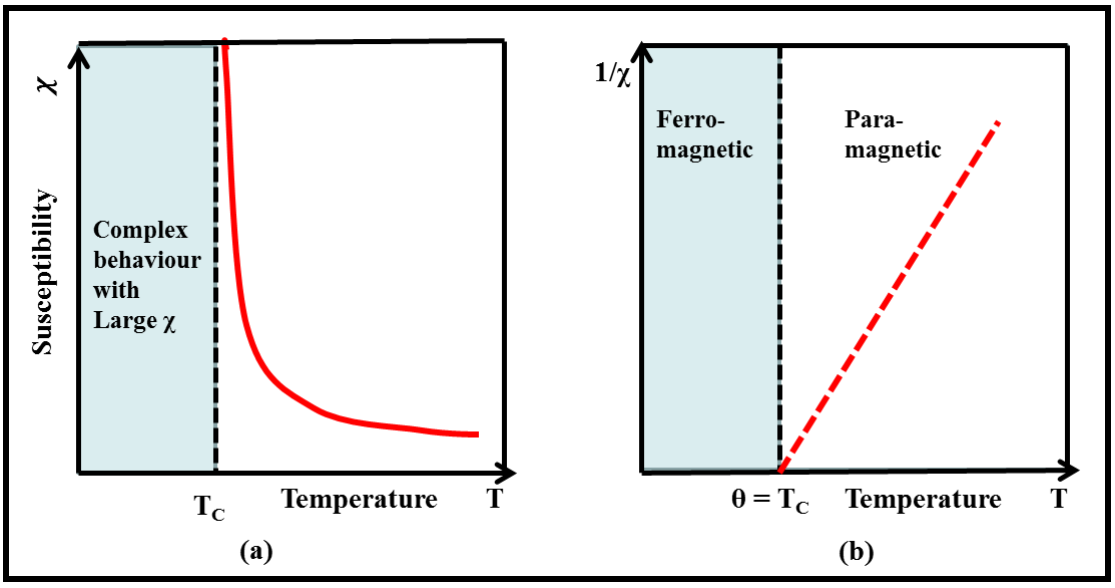

Figure 1.4: *Curie-Weiss law for the ferromagnetic material (a) χ Vs T and (b) χ^{-1} Vs T above and below T_C.*

One of the significant characteristic properties of the ferromagnetic material below T_c is the relation between magnetization M and the applied field H. The loop between M and H is called the hysteresis loop as depicted in figure 1.5. Initially, at point O, the ferromagnetic

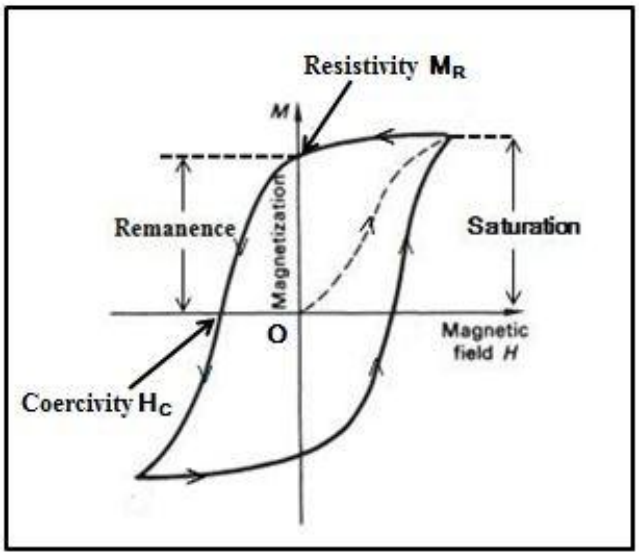

Figure 1.5: *Magnetization M versus applied field H for a ferromagnetic material (Hysteresis loop)*

material is demagnetized. As the magnetic field increases positively, so does the net magnetization of the sample, until all domains are aligned in the direction of field. On removal of applied field, it gives non-zero magnetization. Certain domain alignment processes are irreversible after saturation, and a finite value of magnetization exists when the magnetic field is reduced to zero. Such magnetization is known as remanent magnetization (M_R). When the field is applied in reverse direction, the net moment returns to zero at the point gives coercive field (H_C). If the field is swept further, M(H) curve will eventually map out a hysteresis loop [46][47]. The hysteresis loop includes material

information that ranges from microscopic interactions between individual moments to micron-level domain activity to entire size and morphology of the sample.

Antiferromagnetism

The molecular field theory developed by Neel is used to describe the principle of antiferromagnetism. The domain structure of antiferromagnetic compounds consists of two interleaved sublattices. Moment of each sublattice is ferromagnetically aligned. The magnetic moment of the first sublattice is polarized in one direction, whereas in the second sublattice the magnetic moment is polarized in opposite direction by an equal number. At temperatures below T_N, Neel temperature, antiparellelism gets stronger, and at 0K, the antiparallel arrangement is perfect, as illustrated in figure 1.6(a). Antiferromagnetic materials have no net spontaneous magnetization and can only gain a moment in the presence of strong field. Above T_N, susceptibility follows the equation

$$\chi = C/(T + \theta) \qquad [1.2]$$

Thermal energy is enough to disrupt individual moments and lead them to become paramagnetic over a Neel temperature, T_N. When the antiferromagnetic alignment increases below T_N, the susceptibility starts decreasing. The susceptibility getting close to zero when fields are applied parallel to the ordering vector as shown in Figure 1.6(b) and (c). Unlike the ferromagnetic materials, the antiferromagnetic materials do not show infinite susceptibility at $T=T_N$. This type of magnetism was first observed in MnO crystals. The complications of this type of material is that there are several manners of arranging an identical number of up and down spins depending on the type of crystal lattice on which the spins are to be placed. These arrangements of spins result in different types of antiferromagnetic (AFM) ordering such as A, C and G types as shown in figure 1.7**.** In A-

type antiferromagnetism, the coupling between inter-planes is antiferromagnetic and intra-planes are ferromagnetic, while in the case of C-type, intra-plane coupling is AFM and inter-plane coupling is FM. G-type includes both intra- and inter-plane coupling results a material which is AFM in nature [48].

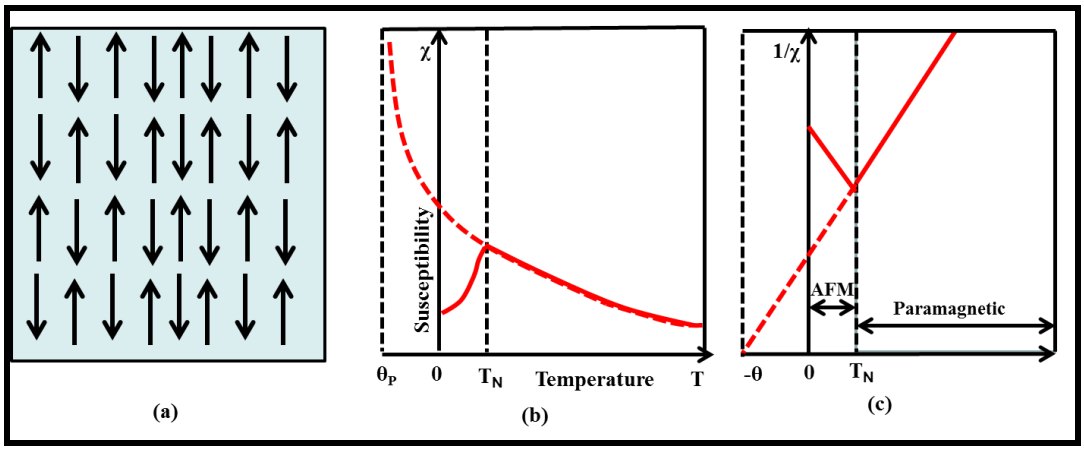

Figure 1.6: *(a) Outline of magnetic dipoles in antiferromagnetic material aligns in opposite direction, Curie-Weiss law (b) χ Vs T and (c) χ^{-1} Vs T above and below T_N.*

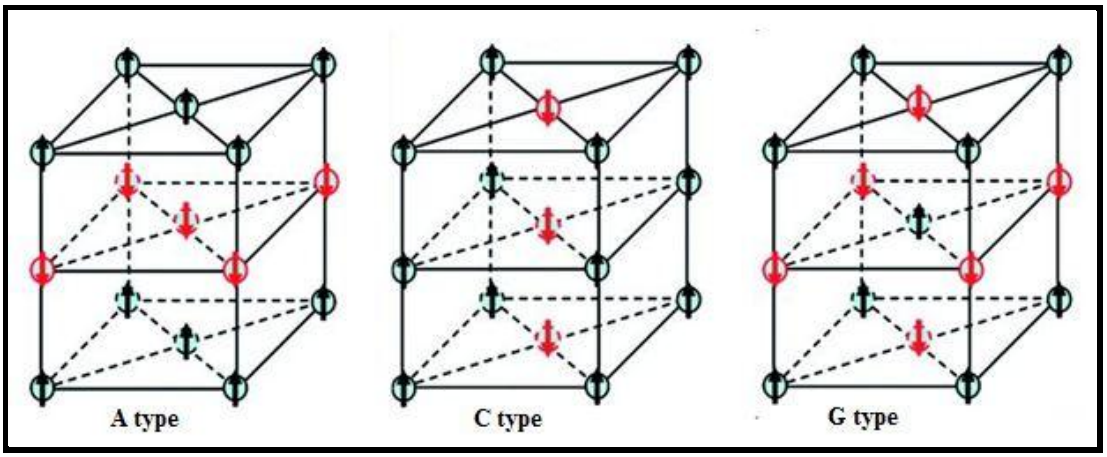

Figure 1.7: *Arrangement of spins in different types of antiferromagnetism.*

Spin-glass: Experimental Phenomenology

Spin-glasses are the class of disordered magnetic materials. The interaction between magnetic impurities in a non-magnetic matrix makes them become spin-glass. Such magnetic systems have mixed interactions characterized by the freezing of spins at well-defined temperature T_f called spin freezing temperature. When the interaction is positive, two spins prefer to align in same direction and create a ferromagnetic bond; otherwise, they align in opposite direction to form antiferromagnetic bond. Because magnetic impurities or ions are dispersed randomly, they can have either a positive or negative charge. At low concentration, there is a large distance between the pairs of ions; therefore, the intensity of the positive and negative interactions is approximately same. For example, in CuMn alloy, low Mn concentration results in both ferromagnetic and antiferromagnetic interactions. As a result, the ferromagnetic and antiferromagnetic bonds are competing with each other and the system becomes frustrated. Due to the randomness, there is a distribution of the distance between the spins results the frustration and thus shows a spin-glass behavior [49], [50].

Spin-glass samples have irreversible behaviour below T_f and reversible behaviour above T_f. Field cooling (FC) produces smooth reversible curves below T_f, whereas zero-field cooling (ZFC) produces irreversible behaviour that gradually relaxes to FC behaviour. The main experimental signs of spin-glasses are as follows:

- At zero-field cooling, the specific heat exhibits a wide maximum of around $1.4T_f$, followed by a gradual decline at high temperature. The peak becomes flat on the application of external magnetic field.

- At T_f, the dc susceptibility curve shows a sharp peak that is highly influenced by magnetic fields, and even a slight increase in magnetic field can smooth it down.
- In comparison to the behaviour of traditional ferromagnets or antiferromagnets, the AC magnetic susceptibility peak shifts with frequency.

Magnetic Interactions

The magnetic behaviour of a magnetic system is determined based on the different exchange interactions among the different atoms. These interactions are categorized into two categories: direct interaction and indirect exchange interaction between spins.

Direct Interaction

Heisenberg's exchange integral is often used to explain such interactions.

$$H = -\frac{1}{\hbar^2} J_{ij}.\ \hat{s}_1.\hat{s}_j \qquad [1.3]$$

where, J is the exchange integral and $\hat{s}_1$ and $\hat{s}_j$ represent the electronic spin of i^{th} and j^{th} atomic sites, respectively with values +1/2 and -1/2. If J_{ij} is positive, the parallel orientation of spins is preferred, indicating that the material is FM in nature [51][52]. If J is negative then material is antiferromagnetic in nature. Direct exchange interaction can be explained through Pauli's Exclusion Principle. Let us take two atoms, each have only one electron. Columbic interaction is minimal when two atoms are brought closer to one another and the electrons may travel in between the nuclei. The Pauli principle requires that the entire wave function must be antisymmetric concerning the interchange of electrons. There is the combination of the spatial wave function and spin wave function with at least one of symmetry of the total wave function must be antisymmetric. Due to this antiparallel alignment, antiferromagnetic ordering exists with a negative value of exchange interaction (J). When these atoms are brought far away from each other, electrons can move away

from the nucleus to reduce the electron-electron columbic interaction. This results in parallel alignment of the spins with a positive value of J i.e. ferromagnetic ordering. The nature of direct exchange interaction can be determined with the help of the Bethe-Slater plot as shown in figure 1.8.

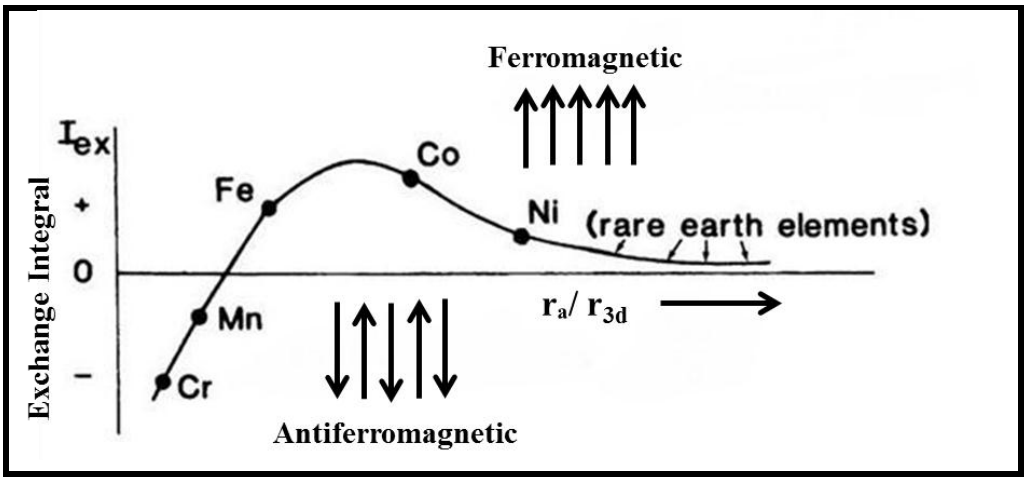

Figure 1.8: *Bathe-Slater curve showing the variation of exchange integral with 3d orbital radius r_{3d} relative to atomic radius r_a.*

Indirect Interaction

(a) Super Exchange Interaction

Indirect superexchange interaction involves the interaction between two nearest neighbour cations such as O^{2-}, S^{2-}, Se^{2-}, Cl^{1-} or Br^{1-} with non-magnetic ions (Oxygen). The 3d orbitals of the transition metal oxides (TMO) are good examples of such interaction. In TMO, ions overlap with the p-orbitals of oxygen. Indirect d-d coupling is known as superexchange as shown in figure 1.9(a). For example, take a system of two magnetic atoms with a single d-

electron, separated by oxygen atom i.e. MnO_2. The hybridization occurs between 3d-Mn orbital and 2p-O orbital which reduces the energy of the system due to the virtual hoping of O-2p electron to the overlapping of Mn d-orbitals. If the transition metal ions makes an angle of around 180° via bridging oxygen, this overlap results in an AFM interaction between the 3d orbitals. The coupling becomes ferromagnetic as the angle approaches 90 degrees and this is the Anderson-Goodenough-Kanamori rules.

(a) Double Exchange Interaction

The coupling of two localized magnetic moments via an nomadic "extra" electron that can move in between two magnetic nuclei is referred to as a double exchange (DE) interaction. It belongs to the spins of magnetic ions with the compounds having mixed valency and is distinguished by a high degree of electron delocalization. Double exchange creates a significant spin polarization effect that favours ferromagnetic spin alignment since the itinerant electron retains its spin orientation during the transfer. This model is comparable to the superexchange model.

In superexchange, an AFM or FM alignment takes place between two atoms having the same number of valance electrons, however in double exchange, the interaction occurs only when one of the atoms has one more electron then the other. *Wang et al.* proposed the initial notion of this indirect transfer based on the electron-spin interaction mechanism to explain the FM seen in the manganites structure of mixed valency, such as $(La_xCa_{1-x})(Mn^{+3}Mn^{+4}_{1-x})_{03}$ [53]. When a La^{3+} ion is replaced by Ca^{2+} ion, one of the Mn^{3+} must drop an electron and become Mn^{4+} to conserve the charge. The electrons on Mn^{3+} ion can jump to a neighboring site of Mn^{4+} via oxygen by interacting with 2p electrons of O^{2-}. This is possible only if there is a vacancy of the same spin. The d-band of the Mn^{3+} ion has four

electrons. These levels are degenerate in a free atom. The degeneracy is lifted after the ion has been put in the oxygen octahedron, as in MnO_2 structure. The levels of an unperturbed octahedron are divided into a doublet known as e_g and a triplet known as t_{2g}. However, due to the strong Hund's coupling, the three electrons at the t_{2g} level want to keep the e_g electron aligned to them. Thus it is not energetically favorable for an e_g electron to hop to an adjacent ion where the t_{2g} spins will be antiparallel to the e_g electron. FM arrangement of neighboring ions is required to retain the high-spin arrangement of both the receiving and the donating ions. The FM originates in such systems is governed by the double exchange (DE) mechanism and can be understood considering figure 1.9(b).

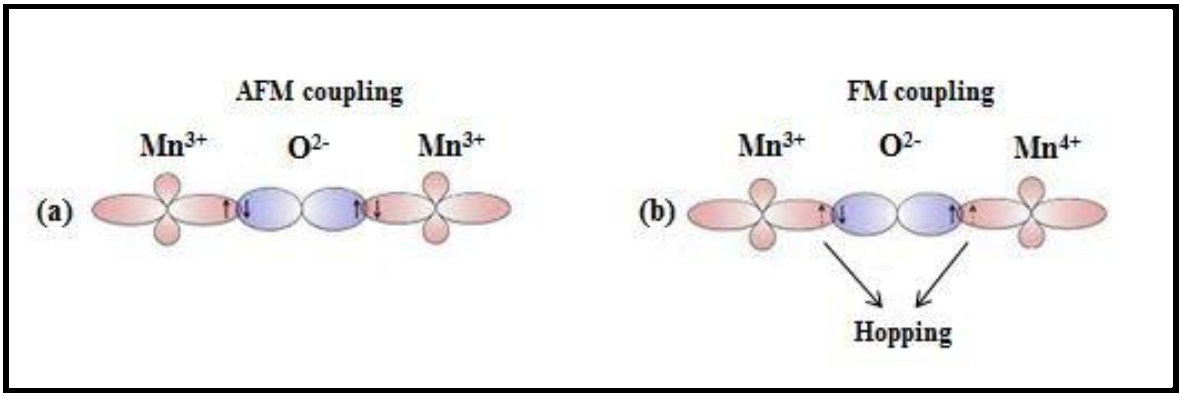

Figure 1.9: *Schematic diagram for (a) superexchange interaction and (b) double exchange interaction.*

Ferromagnetism in Antiferromagnetic Nanoparticles

In general, when the size of the antiferromagnetic particle is reduced, the ferrimagnetic component of the total magnetization becomes visible. According to Neel, there is an appearance of uncompensated spins on the surfaces of the nanoparticles. However, because

of exchange interactions with neighbouring atoms, the spins of uncompensated atoms would still be connected to the underlying order, but these interactions would be reduced by decreasing the coordination of surface atoms. Because of defects, bulk uncompensated spins must exist alongside surface uncompensated spins. This means that antiferromagnetic particles have three different components, diamagnetic, typical AFM and FM component that contribute towards the overall moment of the particle [54][55]. Diamagnetic component is smaller in comparison to others and exists in all type of samples. The second is the typical antiferromagnetic and ferrimagnetic component. In theory, the Curie temperature (T_c) of ferrimagnet material should be same as the Neel temperature (T_N) of an AFM material. If there is strong exchange coupling between the compensated bulk and uncompensated surface moments, we may expect the ferrimagnetic moment to drop with dropping temperature, as it does in an AFM. Higher-complexe exchange coupling should act more like ferromagnets, with the total moment increasing with decreasing temperature.

1.1.3 Applications

When numerous key features in the practical application of nanomaterials, for example abundance in nature, low cost, nontoxic, and environmental benignity, are taken into account, manganese dioxide (MnO_2) attracts special interest from researchers and has been employed in a variety of applications [56][57]. It also has distinct characteristics because of multiple valence states of manganese (+2, +3, +4, and +7). Figure 1.10 depicts a handful of the many characteristics of MnO_2. These characteristic properties make it a promising and functional nanomaterial in environmental purification systems, as a catalyst [58], absorbent of noxious elements [59], sensors [60], dry cell batteries [61], [62], inorganic coloring of ceramics [63], electrodes for Li batteries [64][25], Na batteries [65], Mg batteries [66] and

supercapacitors [67][68](Figure 1.11). MnO_2 is also frequently utilized as an electrode in alkaline batteries, as a photocatalyst, and in electrolysis [69]–[71]. MnO_2 has the capacity to absorb harmful ions, which has led to its usage in important water cleaning applications [72]. Manganese dioxides are non-stoichiometric compounds because it absorbs water molecules and other cations to stabilize its structure. However, due to a number of drawbacks, the material's unsatisfactory efficiency has so far hampered its further application. Nanosized MnO_2 particles agglomerate easily during the adsorption or catalytic reaction process due to their high surface energy. Due to their extremely narrow bandgap, recombination is a risk for photoinduced electrons and holes, which limits their application in photocatalysis.

MnO_2 as an Electrode in Supercapacitor

Supercapacitors are electronically charged devices that can hold massive quantities of electric charge. Supercapacitors are classified into three types based on their energy storage method, as seen in Figure 1.12. The first is the electrode double layer capacitor (EDLC). Capacitance is achieved in this group due to the accumulation of pure electrostatic charge on the electrode-electrolyte interface. This group is heavily reliant on the amount of electrode surface area available to electrolyte ions. Second one is the pseudocapacitor. Due to electro-active species, a fast and reversible faradic process occurs in this case, as illustrated in figure 1.13 [56][73][11]. Hybrids are a third group that combines the properties of both EDLCs and Pseudocapacitor devices. Electrical properties are determined by the electrode material used in supercapacitors. It is a surface process to store charge in two layers on the same surface. Surface properties of electrode materials have a significant impact on the capacitance of a cell.

A supercapacitor is made up of an electrode, an electrolyte, and a separator, with the electrode being crucial to its performance. Exploring electrode materials with excellent performance is a critical task. When it comes to the workings of pseudo-capacitors, it's

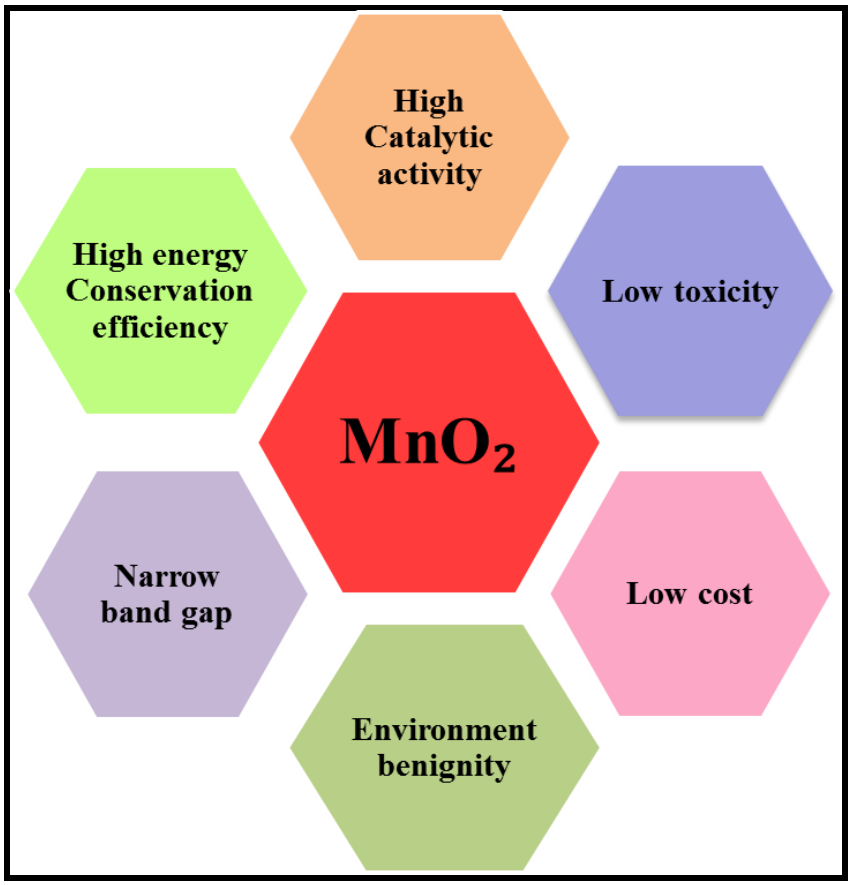

Figure 1.10: *Various properties of MnO_2 nanostructures.*

important that the electrode materials and electrolytes make good contact, and that ions/charges move quickly both inside and outside of the electrode. As a result of their large specific surface area and suitable pore dimensions, transition metal oxides with mesopores (between 2 and 50 nm) are advantageous for the construction of high-

performance supercapacitors. Mesoporous compounds like RuO_2[74] , MnO_2 [75], ZnO [76], Fe_2O_3 [77], and $NiMn_2O_4$ [78] have been explored extensively for their potential application in supercapacitors during last decade. Among other TMOs, RuO_2 comprises redox reaction induced charge transfer processes, and the shape of its cyclic voltammogram (CV) curve is extremely wide, with a quasi- rectangular form. Fast and reversible redox reactions with high capacitance are aided by good conductivity, quick charge transfer and a larger specific surface area. Unfortunately, high price and toxicity of RuO_2 restrict it from being used on a wide basis. MnO_2 has a low-cost and rectangular voltammogram as a result of fast and reversible faradaic reactions, making it one of the promising alternatives to RuO_2.

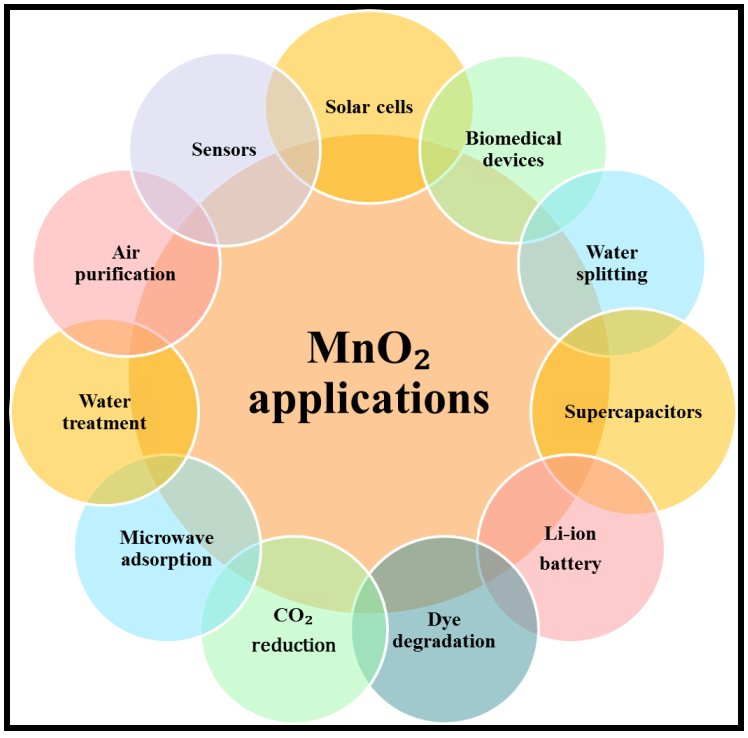

Figure 1.11: *Different applications of MnO_2 nanostructures.*

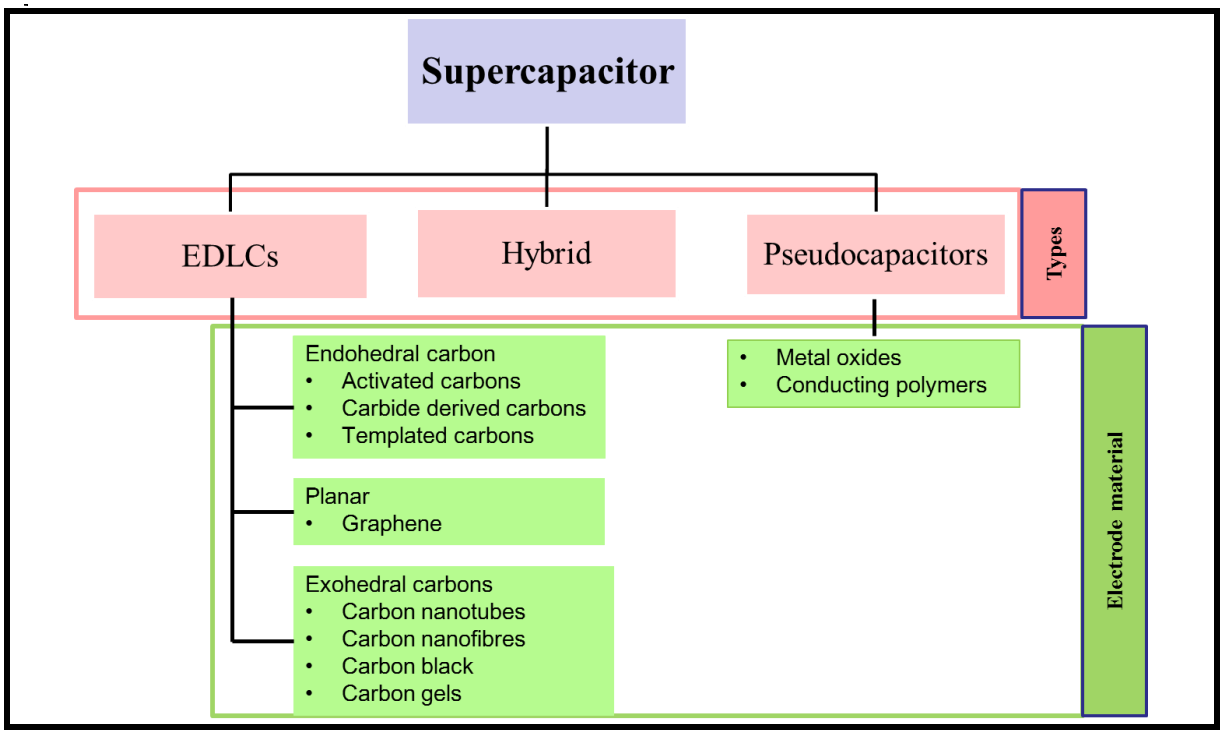

Figure 1.12: *Taxonomy of materials for supercapacitors.*

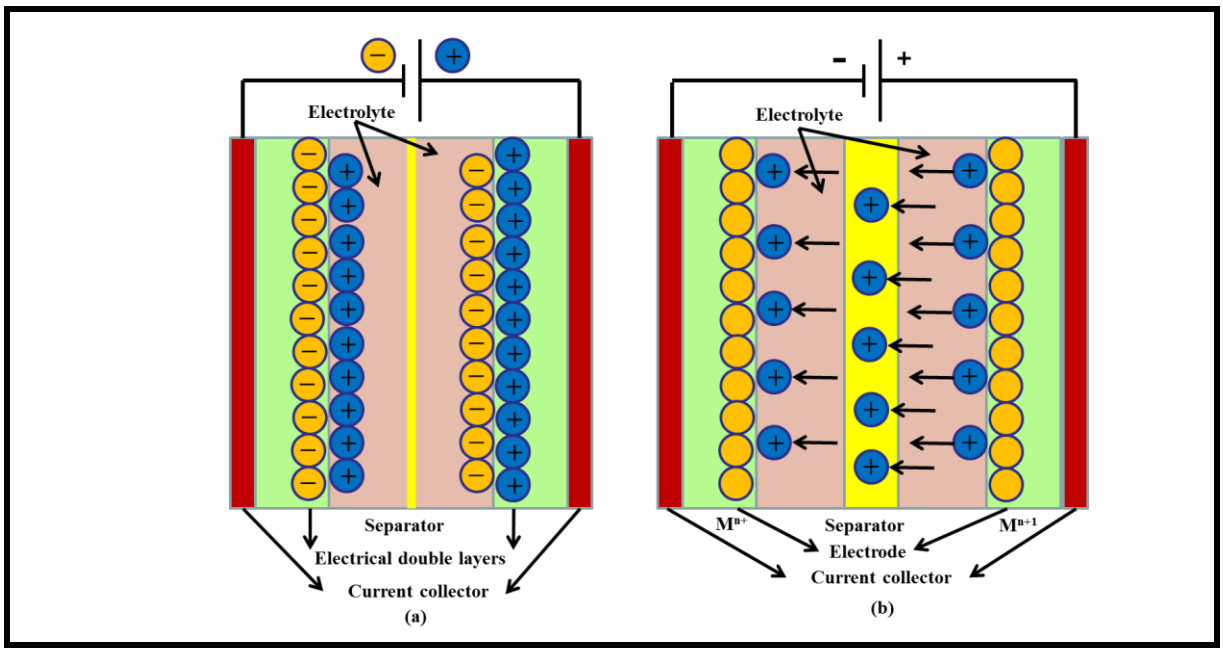

Figure 1.13: *Schematic diagram of supercapacitor (a) EDLC and (b) Pseudocapacitor.*

In 1999, Goodenough has reported the first use of MnO_2 as an electrode in supercapacitors [79]. This discovery opened up new possibilities for the development of the range of electroactive MnO_2 electrodes for high performance supercapacitors. This is due to the fact that MnO_2 has several benefits over other materials. Its theoretical specific capacitance is 1370 Fg^{-1}, a 1.0 V working potential window, and the capacity to permit electrolytes with considerably less chemical corrosion to current collectors [80]. For improved electrochemical performance, there should be a tuning between the crystalline and amorphous nature of an electrode material. The electrochemical performance of an amorphous structure is superior to that of a well-crystallized structure.

The Charge Storage Mechanism

It involves a reversible intercalation and deintercalation of protons or ions into/from MnO_2 lattice as well as a transition of Mn^{3+} to Mn^{4+} and vice versa. The charge/discharge process involves two sorts of mechanism involved in the reaction. The first is the cation adsorption and desorption on the surface of MnO_2. It depends on the radius and mobility of the ions [81]. Second one is the intercalation/deintercalation of cations/protons into/from bulk MnO_2, expressed as

$(MnO_2)surface + M^+ + e- \rightarrow (MnOOM)surface$

$MnO_2 + M^+ + e- \rightarrow MnOOM$

where M^+ signifies alkali cations, like Li^+, Ba^+, and K^+.

As a result, the charge storage method is linked not only to MnO_2 frameworks, but also to other variables including surface area, electronic and ionic conductivity among others.

Factors Affecting the Pseudocapacitance of MnO_2 Electrode Materials

Exploring the optimum crystallinity with excellent conductivity and ionic transport is both essential and challenging. It is observed that electrochemical capacitance strongly depends on the crystallographic structure in the order of α-$MnO_2 \geq \delta$-$MnO_2 > \beta$-MnO_2 [82]. As a result, the crystallinity, shape, surface area, diffusion, and size of the nanoparticles all play crucial role in the supercapacitive performance of MnO_2 [56]. Therefore, much effort has gone into developing MnO_2 polymorphs with a variety of morphology and huge surface area. MnO_2 has low electronic conductivity i.e. ~ 10^{-5} to 10^{-6} S cm^{-1} [83], which is responsible for its low experimental specific capacitance, usually upto 350-400 Fg^{-1} which is quite smaller than the theoretical value of 1370 Fg^{-1} [83]. Thus, to achieve ideal supercapacitive performance, it is important to improve the conductivity of MnO_2 with large surface area. One effective approach is doping metal cation into the MnO_2 matrix or composing it with highly conductive carbon materials and conductive polymers.

1.2 Literature survey

1.2.1 Synthesis of the Polymorphs of MnO_2

Nanostructured MnO_2 samples with varied controllable morphologies are being synthesised using a variety of techniques. Using different methods, one can readily regulate the size, shape, and growth of the nanoparticles by adjusting the synthesis parameters. The majority of the common methods used in the synthesis and functionalization of MnO_2 nanoparticles are simple reduction, co-precipitation, microwave, sol-gel, reflux root, and the hydrothermal synthesis technique.

In the sol-gel method, the formation of gel takes place via the redox reaction of potassium permanganate with carboxylic acid such as citric acid, fumaric acid etc. [84]. Formation of different tunnel size MnO_2 structures are controlled by adjusting the pH of the gel. For instance, α-phase of MnO_2 is formed in conc. acid, while δ-MnO_2 is produced in the conc. base [84][85]. Nanowires of α- and β-MnO_2 are synthesized through the oxidation of Mn^{2+} cations by $S_2O_8^{2-}$ ions in an aqueous solution without using any catalyst in sol-gel method [85]. A low temperature sol-gel method uses manganese acetate tetrahydrate $(CH3COO)_2Mn.4H_2O$ and conc. HNO_3 accompanying with different surfactants in alcoholic solvent. MnO_2 nanowires and nanorods are synthesised in the presence of polyvinyl pyrrolidone (PVP) and cetyltrimethylammonium bromide (CTAB), respectively [86].

In coprecipitation technique, the advantage over other synthesis methods is the ease with which the particle size and composition can be controlled without a need of any surfactant. This method involves reaction between equal amount of any two manganese salts, like $MnSO_4$ and $C_2H_2MnO_4$, and adjusting the pH to 12 by adding sodium hydroxide to obtain a dark brown MnO_2 precipitate [87]. Co-precipitation of Manganese chloride, $MnCl_2$ and manganese oxalate, $C_2H_2MnO_4$with the addition of NaOH to regulate the pH of aqueous solution results in the formation of α-MnO_2 nanosheets [87]. Urchin-like α-MnO_2 nanomaterials are also synthesised using a simple coprecipitation process of H_2SO_4 and $KMnO_4$ in an aqueous solution heated to 85°C [88].

Subramanian et al. have synthesised a variety of MnO_2 microstructures by tuning the decomposition period of $KMnO_4$ and $MnSO_4$ from 1 to 18 h at 140°C through hydrothermal technique [89]. MnO_2 nanorods, nanosheets and nanotubes are obtained by

Xiao et al. when the same reaction solution is kept at 100-200°C for 12 h [90]. Single crystal of β-MnO_2 nanotubes of diameter 200-500 nm are prepared through hydrothermal technique by the oxidation of $MnSO_4$ with sodium chlorate in the assistanceship of PVP [91]. *Cheng et al*. reported a synthesis of γ-MnO_2 nanowires and α-K_xMnO_2 nanofibers from a reaction of $MnSO_4$ with $(NH_4)_2S_2O_8$ and $KMnO_4$, in an autoclave at 90°C for 24 h and 140°C for 12 h, respectively [74][92].

The microwave Irradiation (MWI) method is one of the simplest and fast methods to synthesis nanostructured materials since there is no need of high temperature or pressure. The ability of a solvent or reagent to absorb microwave radiation determines how quickly a substance is heated by irradiating it with microwave radiation. *Zhang et al.* develop a facile one-pot microwave aided hydrothermal method to synthesise δ-MnO_2 microspheres and nanorods at 60°C and 140°C by the reduction of $KMnO_4$ uder microwave radiation irradiating for 10 min. [93]. Similarly, nanoballs platelike MnO_2/MWCNTs is well synthesized by placing the solution of $MnSO_4$, $(NH_4)_2S_2O_8$ and CNTs in microwave oven for 16 min. [94].

The aqueous-based reflux technique, which is beneficial for the green synthesis of nanostructured materials permits in situ sample crystallization under ambient pressure and temperature under the boiling point of the solvents. To synthesise required phase and morphology of the nanomaterials, the parameters like concentration of precursors, the time of reflux, and the cooling rate should be optimized. *Wang et al*. have used the refluxing technique to produce λ-MnO_2 nanodisk from manganese acetate and PVP in a dimethyl sulfoxide solution [37]. *Cui et al.* have synthesized single-crystalline β-MnO_2 nanorods

using a reflux-root reaction of potassium permanganate and manganese sulphate in HNO_3 solution [34].

1.2.2 Structural Transformation: Effect of Synthesis Parameters & dopants

As MnO_2 has a flexibility to exist in a number of polymorphic forms as α-, β-, γ-, δ- and λ-phase. Phase transformation from one phase to other is crucial from the application point of view. The performance of MnO_2 in a diverse range of applications such as supercapacitors, catalysts, sensors, and so on can be improved if the phase transformation can be well studied. Despite a wide range of reports providing synthesis techniques for MnO_2 polymorphs and their transitions, knowledge of the fundamental driving factors is limited. This gap makes it challenging to distinguish between kinetic and thermodynamic effects in any systematic investigation of the production of MnO_2, as well as to make assessable theory regarding polymorphic transitions which limit both scientific knowledge and design of functional MnO_2-based materials. Many efforts have been made to date to understand the phase and structural transformation of MnO_2 using different synthesis routes.

The additive in the hydrothermal and other synthesis methods is the key to control the process of phase transformation so that the phase content of MnO_2 can be precisely controlled. Moreover, phase transformation significantly depends on the synthesis conditions [95]. For example, *wang et al.* synthesized β-MnO_2 through hydrothermal synthesis technique by a reaction between $MnSO_4$ and $(NH_4)_2S_2O_8$ which on further addition of $(NH_4)_2SO_4$ produces α-MnO_2 [82]. α-MnO_2 nanorods have been successfully synthesized by *Li et al.* via reaction between $MnSO_4$ and $(NH_4)_2S_2O_8$ of equal concentration while on increasing the concentration of both the precursors with same

processing steps, a mixture of α- and γ-MnO_2 is obtained [7]. *Musil et al.* have synthesized various polymorphs of MnO_2 by increasing the reaction temperature by twice using the same reaction conditions [96]. *Wei et al.* transform γ-MnO_2 at room temperature to α- and β-MnO_2 at 140 and 170°C, respectively [91]. δ-MnO_2 is transformed to MnOOH in dodecyl amine solution which again transforms to β-MnO_2 after annealing it at 300°C [97]. *Shen et al.* report a phase transformation of δ-MnO_2 to other polymorphs of MnO_2 by varying the pH from 13 to 1 [98]. *Zhang et al*. have proposed an approach for controlled phase transformation to synthesize different compositions of α/β-MnO_2 by adding zinc acetate as a phase transforming agent as shown in figure 1.14. When the concentration ratio of Zn/Mn increases from zero to $1.75x10^{-3}$, it transforms from α to β-MnO_2 which again forms α-MnO_2 on further increasing the Zn/Mn ratio to $3.85x10^{-2}$ [99]. Extraction/intercalation of external cations in MnO_2 framework also induces phase transformation. This suggests that cations play an important role in kinetical or thermodynamical stabilization of the MnO_2 polymorphs [100]. Phase selectivity depends on the compatibility of the accessible interstitial site with the coordination of alkali ions. As a result, Na^+, Ca^+, K^+ cations stabilize α-MnO_2; Na^+ ions and water molecules stabilized δ-MnO_2 and; Li^+ and Mg^+ ions stabilize λ phase. *Kitcheav et al.* predict an equilibrium thermodynamics driven phase diagram between A_xMnO_2 system and external cation (figure 1.15). They evaluate the thermodynamics of the intercalation of alkali and alkali-earth (A = K^+, Li^+, Na^+, Mg^{2+} and Ca^{2+}) cations into MnO_2 framework and establish a relation for the type and concentration of cation on the stability of the polymorphs of MnO_2. They conclude that α-, *λ*- and δ- structures are not thermodynamically stable and can be stabilized by alkali intercalation. While, all cations except Li prefer δ- phase, Na, Ca and K

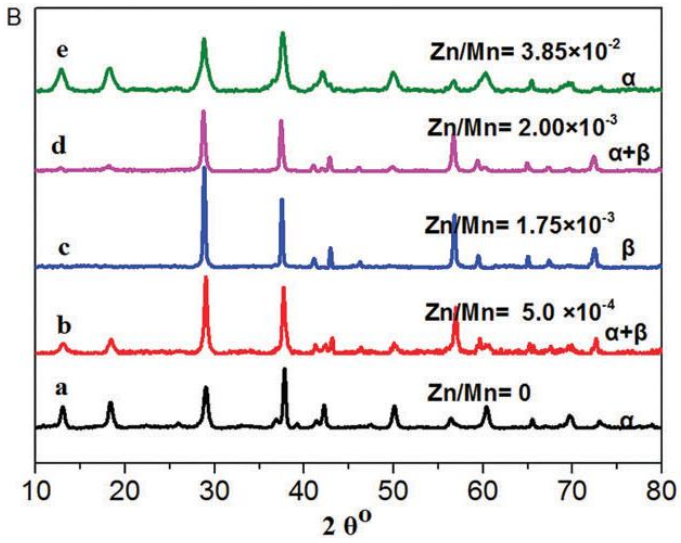

Figure 1.14: *XRD patterns of the different compositions of Zn/Mn mix-MnO_2.*

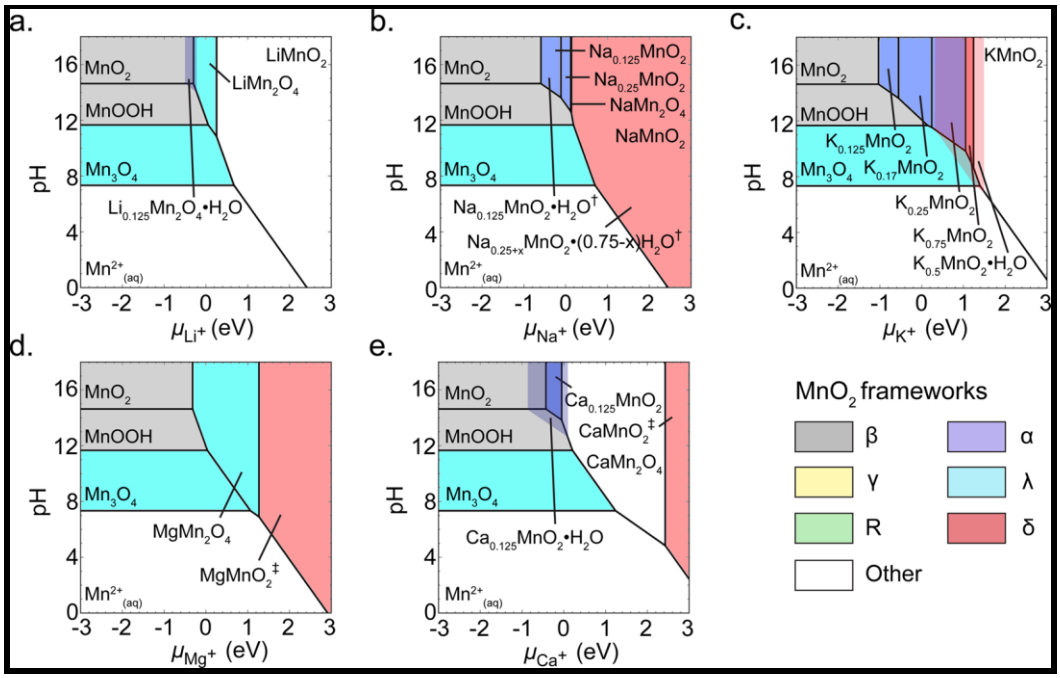

Figure 1.15: *Constrained equilibrium thermodynamics driving phase selection between MnO_2 polymorphs as a function of solution conditions at 298 K and zero applied potential, for solutions containing (a) Li^+, (b) Na^+, (c) K^+, (d) Mg^{2+}, or (e) Ca^{2+} cations.*

cations prefers the formation of α-MnO_2. Spinel structured λ-MnO_2 is favored by Li^+ and Mg^{2+}. R and γ phase are stabilized by Ruetschi defect and proton insertion [33]. *Hastuti et al.* have observed a phase transformation from α-MnO_2 to R-MnO_2 after doping Fe. A large ionic radius of Fe increases the micro-strain and oxygen vacancies that cause tunnel destruction from (2x2) to (2x1) [101]. Hydrothermally synthesized Fe doped MnO_2 leads to a transformation of phase from α-MnO_2 to a mixture of α and ε-MnO_2 [95].

1.2.3 Structure, Morphology and Dopant Dependent Magnetic Properties

Modulating the crystal structure is a possible way to tune the magnetic behaviour as it determines by means of the short range interactions among the magnetic ions, crystallographic characteristics like bond length, bond angle, and coordination ions. Surface reconstruction can also be used to tune these parameters and control the magnetic behaviour and optimize their functional performance for various applications. In this context, *Li et al.* have synthesised MnO_2 nanowires with different exposed planes and investigated their modulated magnetic properties. The exchange bias effect is much stronger in MnO_2-210 as compared to MnO_2-110 and the difference is attributed to their crystal structure [102]. The magnetic characteristics of α-, β-, γ- and δ-MnO_2, synthesized using both hydrothermal and coprecipitation methods illustrate that while α-MnO_2 displays a spin-glass like behaviour below 50 K, β- and δ-MnO_2 exhibit an antiferromagnetic (AFM) transition at 92 K and 20 K, respectively. γ- MnO_2 maintains its paramagnetic state irrespective of temperature range [23]. The morphology related characteristics of nanomaterials have also gained the interest of researchers as a means of generating unusual properties with a high potential for the practical and innovative applications. Rich diversity

in the magnetic characteristics of MnO_2 comes from the variation in composition and structure, which are generated using different synthesis techniques. Depending on the synthesis technique, sputtered grown α-MnO_2 nanorods have shows an exchange bias (H_{EB}) of 1340 Oe for the cooling field of 30kOe [1]. On the other hand, α-MnO_2 nanoribbons synthesized through molten salt method possess a large zero field cooling H_{EB} of 1100 Oe [103]. Furthermore, the complicated magnetic characteristics of MnO_2 are extremely intriguing to study because of their uniquely diverse magnetic ordering. They are most likely produced by magnetic frustrations and the existence of a significant amount of cations inside the tunnels. Cations of alkaline earth elements, and metals, can be doped in the structures due to comparatively large tunnel size. Through careful doping element selection, the characteristics of α-MnO_2 can be modified in accordance its utilization for various applications. AFM behaviour of α-K_xMnO_2 for ($x \leq 0.07$) is observed below 24.5 K [104], however single crystals of α-$K_{0.166}MnO_2$ exhibits an AFM interaction below 18 K [4]. *Tsang et al.* tuned the magnetic characteristics of α-MnO_2 nanotubes by inserting Na^+, Li^{3+}, and K^+ cations inside the tunnels [5]. Incorporation of K cation with varying concentration affect the magnetic interactions present in α-MnO_2 nanotubes. When the concentration of K^+ is less than 12 at%, it exhibits FM ordering, when the doping concentration ≥ 12 at %, it shows AFM ordering [5]. The Neel temperature (T_N) of dandelion type β-MnO_2 has increased to 100 K from 92 K in bulk β-MnO_2. *Barudzija et al*. comprehensively examined the structural and magnetic characteristics of hydrothermally synthesised β-MnO_2 and α-K_xMnO_2 (x = 0.15 and 0.18) [6]. β-MnO_2 nanorods exhibits an antiferromagnetic ordering at 93 K, while both α-K_xMnO_2 (x = 0.15 and 0.18) nanorods exhibit reentrant spin-glass (RSG) feature at freezing temperature, 21 K and 20 K,

respectively. *Zhou et al.* reported that α-MnO_2 shows SG like characteristic below 50 K, and β- and δ- MnO_2 shows an AFM transition at 92 K and 20 K, respectively. On the other hand, γ-MnO_2 maintains paramagnetic behaviour during the entire temperature range from 300 K to 0 K [39]. *Yu et al.* demonstrated that Ba doped α-MnO_2 nanoribons exhibits an exchange bias of 865 Oe for zero foeld cooling [2].

1.2.4 MnO_2 as an Electrode Material for Supercapacitor application

Among all polymorphs of MnO_2, α-phase is considered to be the suitable phase from application point of view as it has a large tunnel size which may intercalate external cation to alter the properties of MnO_2. Therefore, α phase is more electrochemically active phase in comparison to other phases. Although, other phases of MnO_2 are also electrochemically active. *Zhao et al.* have synthesized α-MnO_2 nanourchins through hydrothermal method at 80, 110 and 140 °C. Among them, α-MnO_2 synthesized at 110°C owns poor crystallinity in comparison to other. α-MnO_2 nanourchins possess the highest capacitance of 155.5 Fg^{-1} at $1Ag^{-1}$ [105]. α-MnO_2 nanowires with poor crystalline nature possess high specific capacitance with high stability compared to highly crystalline α-MnO_2 nanorods [106]. *Yin et al.* have synthesised different phases of MnO_2 and study the variation in their electrochemical performance. They observed that specific capacitance decreases in the order of α-MnO_2 (535 F/g) > δ-MnO_2 (464 F/g) > β-MnO_2 (155 F/g) [107]. A structure controlled synthesis of α and β-MnO_2 nanorods, γ-MnO_2 urchin-like microspheres, δ-MnO_2 nanowire and nanosheet have been synthesised by *Wang et al*., and have observed that, at 5 mVs^{-1}, the γ-MnO_2 microspheres, α- MnO_2 and β-MnO_2 nanorods have capacitance 237.6,

Table 1.2: Polymorphs of MnO_2 with different morphologies and their specific capacitance.

Phase structure	**Morphology**	**Electrolyte**	**Specific capacitance**	**Reference**
β-MnO_2	Nanorods	3M KOH	125 Fg^{-1} at 1 Ag^{-1}	[108]
δ-MnO_2	Nanosheets	1M Na_2SO_4	300 Fg^{-1} at 1 Ag^{-1}	[109]
MnO_2	Hierarchical hollow nanoparticles	1M Na_2SO_4	308 Fg^{-1} at 0.2 Ag^{-1}	[110]
α-MnO_2@ δ-MnO_2	Snowflake like coreshell	1M Na_2SO_4	260.5 at 0.3 Ag^{-1}	[111]
δ-MnO_2	Porus Nanotube	1M Na_2SO_4	365 Fg^{-1} at 0.25 Ag^{-1}	[112]
β-MnO_2	Nanowires	1M Na_2SO_4	453 Fg^{-1} at 0.5 Ag^{-1}	[113]
δ-MnO_2	Ultrathin tremella-like structure	1M Na_2SO_4	220 Fg^{-1} at 0.1 Ag^{-1}	[114]
δ-MnO_2	Nanoflower	1M NaOH	256.5 Fg^{-1} at 0.3 Ag^{-1}	[115]
Single crystal α-MnO_2	Nanotube	1M Na_2SO_4	220 Fg^{-1} at 5 mVs^{-1}	[116]
δ-MnO_2	Nanoplates	2M Na_2SO_4	165 Fg^{-1} at 5 mVs^{-1}	[117]

103.9 and 57.7 Fg^{-1}, respectively [8]. Table 1.2 shows the speficpacitance of different phases of MnO_2 with their morphology.

Doped MnO_2 Nanostructures

One of the most significant ways for modifying the physical and chemical characteristics of functional materials is doping. Control over doping can increase the ionic and electronic conductivity of MnO_2. MnO_2 is a semiconductor material with high resistance (10^5-10^6)

Ωcm which limits its better electrochemical performance. Therefore, doping may offer a high specific capacitance or lead to a phase transformation. For example; *Poonguzhali et al.* observed an enhancement in SC from 210 Fg^{-1} to 912 Fg^{-1} after doping Fe in α-MnO_2 [118]. Vanadium doped δ-MnO_2 nanosheet display an excellent electrochemical performance as supercapacitor electrode because of significant increase in its electronic conductivity [119]. Cu doped β-MnO_2 is a potential cathode for Li-ion batteries with excellent cyclic stability of 125 $mAhg^{-1}$ after 100 cycles [119]. *Tang et al.* report that after doping Co in MnO_2, the specific capacitance of 350 Fg^{-1} is achieved at a current density of 0.5Ag^{-1} which is quite higher than the specific capacitance of pure MnO_2 (168 Fg^{-1}) (figure 1.16) [9].

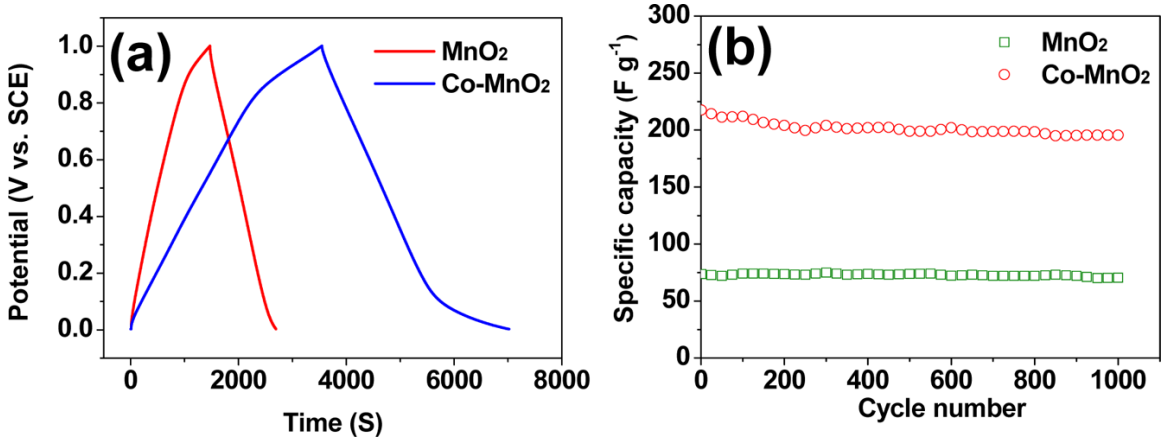

Figure 1.16: *(a) Galvanostatic charge/discharge curves of MnO_2 and Co-MnO_2 spheres at a current density of 1 A/g (b) cyclic stability of MnO_2 and Co-MnO_2 at a current density of 2 A/g.*

Cryptomelane (α-$KxMnO_2$) can be made to have novel morphologies and electrochemical properties by changing the crystal chemistry and replacing K^+ ions by a metal cation with either a low valency (+3, +2, +1) or a high valency (+5, +6). The metal cation can be intercalated or doped into MnO_2 lattice in two possible ways. One method is to replace the Mn cation in MnO_6 octahedra with a cation (six-coordinate cation) of radius similar to Mn^{3+} low spin (0.72), Mn^{3+} high spin (0.785), and Mn^{4+} (0.67) and the other method is to insert dopant cation within (2 x 2) tunnels with a crystal radius similar to K^+ (1.65), which results in eight-coordination cation [120]. Lower valence dopant cations can make lattice more negative, which encourages the insertion of additional K^+ cations within the tunnels and increases the stability of the structure. High-valency dopant cations generate an excess of electrical charge, which is balanced by the formation of vacancies, resulting in deformation of structure and thermal instability. It has been observed that MnO_2 framework doped with metal cations like Ag^+, Ni^{2+}, Cu^{2+}, Co^{2+}, Fe^{3+}, Cr^{3+}, Mo^{6+}, V^{5+}, W^{6+}, etc., successfully increases the specific capacitance as illustrated in table 1.3.

Recently, rare earth (RE) based nanostructures and their composite have progressively gains the interest of researchers. Because of their unpaired 4f electronic configuration they can readily control the structural characteristics while maintaining the excellent physical and chemical properties. Most of the rare-earth elements such as Ce, Er, Nd, Pr, Sm, etc. exhibit RE^{3+}/RE^{2+} or RE^{4+}/ RE^{3+} redox couple which shows that they are also feasible for electrochemical energy storage. [121]–[124]. Nanostructured RE based materials have high surface to volume ratio. This indicates that they have more number of active sites which can participate in redox reactions and hence increases the capacitance. The pseudocapacitive performance of MnO_2 nanostructures may be tuned by combining MnO_2

Table1.3: Comparision of specific capacitance of cation-doped-MnO_2 nanostructures reported in literatures.

Electrode material	**Morphology**	**Electrolyte**	**Specific capacitance**	***Reference***
Ag doped MnO_2	Nanosheets	1M Na_2SO_4	272 Fg^{-1} at 10 mVs^{-1}	[125]
Co-doped MnO_2	Yolk shell spheres	1M Na_2SO_4	196 Fg^{-1} at 2 Ag^{-1}	[9]
Cu doped δ-MnO_2 thin film	Microspheres	LiCl-PVA gel electrolyte	300 Fg^{-1} at 5 mVs^{-1}	[10]
2at% Fe doped MnO_2 thin film	Nanonest	1M Na_2SO_4	273 Fg^{-1} at 5 mVs^{-1}	[126]
0.1M Cu doped MnO_2	Nanocrystals	0.5M KCl	583 Fg^{-1} at 10 Ag^{-1}	[127]
Fe doped MnO_2	Hollow urchin-like architectures	1M Na_2SO_4	203.3 Fg^{-1} at 0.25 Ag^{-1}	[128]
1at% Ni-doped MnO_2	Nanospheres	0.5M Na_2SO_4	451 Fg^{-1} at 5 mVs^{-1}	[129]
Cu doped MnO_2	Porus microspheres	1M Na_2SO_4	365 Fg^{-1} at 1 Ag^{-1}	[130]
5% Co doped MnO_2	Nanowire	1M Na_2SO_4	415 Fg^{-1} at 0.2 Ag^{-1}	[131]
Sn doped σ-MnO_2	Hollow nanostructures	0.5M Na_2SO_4	169.9 Fg^{-1} at 1 Ag^{-1}	[132]
0.125M Zn doped MnO_2	Spherical particles	0.5M KCl	620 Fg^{-1} at 10 mVs^{-1}	[133]
Fe doped δ-MnO_2	Nanoneedles	3M KOH	627.3 Fg^{-1} at 1 Ag^{-1}	[134]
Zn doped δ-MnO_2	Nanoflakes	1M Na_2SO_4	466 Fg^{-1} at 0.5 Ag^{-1}	[36]
B doped MnO_2	Nanosheet	0.5M Na_2SO_4	269 Fg^{-1} at 50 mVs^{-1}	[135]
1.5at% Er doped α-MnO_2	Microspheres	0.5M Na_2SO_4	224.3 Fg^{-1} at 0.5 Ag^{-1}	[136]
Sn doped α-MnO_2	Nanoflower	1M Na_2SO_4	243.6 Fg^{-1} at 1 Ag^{-1}	[137]

with rare earth elements. For example, doping of La/Ce in MnO_2 enhances the capacitance from 466 to 608 F/g at a scan rate of 10 mV/sec [138]. Chen et al. have observed that after doping Ce+ ion in β-MnO_2 transforms it to an electrochemically active phase α-MnO_2 [107].

Table1.4: Comparision of the specific capacitance of MnO_2 nanocomposites reported in the literature.

Electrode material	Electrolyte	Specific capacitance	Stability (cycles)	Reference
MnO_2@GO	1M Na_2SO_4	307.7 Fg^{-1} at 0.1 Ag^{-1}	-	[139]
MnO_2@HGO (holey Graphene oxide)	1M Na_2SO_4	117.48 Fg^{-1} at 5 mVs^{-1}	-	[140]
MnO_2@g-C_3N_4 (graphic carbon nitride)	0.5M Na_2SO_4	211 Fg^{-1} at 1 Ag^{-1}	100% (1000)	[141]
MnO_2@NRGO (Nitrogen doped graphene oxide)	0.5M Na_2SO_4	522Fg^{-1} at 2 mVs^{-1}	96.3% (4000)	[142]
MnO_2@Graphite nanoplatelet	2M $(NH_4)_2SO_4$	276.3Fg^{-1} at 2 mVs^{-1}	93% (10)	[143]
MnO_2@MCNT	1M KOH	250.5 Fg^{-1} at 2 mVs^{-1}	-	[144]
MnO_2@Graphene	1M KCl	328 Fg^{-1} at 1 Ag^{-1}	99% (1300)	[145]
MnO_2@PANI@MCNT	1M KOH	348.5 Fg^{-1} at 1 Ag^{-1}	88.2% (2000)	[146]
MnO_2@PPY	1M Na_2SO_4	303 Fg^{-1} at 20 mVs^{-1}	71.2% (500)	[147]
PANI@MNO_2@PCNF (Porus Carbon nanofibers)	1M H_2SO_4	289 Fg^{-1} at 1 Ag^{-1}	91% (1000)	[148]

MnO_2 Based Nanocomposites for High Performance Supercapacitors

An ideal nanocomposite electrode material to be used in supercapacitors should be composed of a high power and energy density material (carbon-based compounds and MnO_2). Carbon based samples possess high surface area and electronic conductivity that can be used to facilitate charging channels. These channels can improve the rate capability of MnO_2. Pseudocapacitive materials are composed of conducting polymers which provides good electronic conductivity for MnO_2 by interlinking the polymer chains with MnO_2. Such interlinking of polymer chains provides a percolated electrical conducting pathway with an improvement in charge exchange efficiency that also provides the stability during redox process. A strong synergistic effect is likely to emerge in MnO_2/conducting polymer due to the high pseudocapacitance of both components. Carbon nanotubes (CNTs), carbon nanofibers (CNFs), graphene, and carbon nanofoams etc. are used to make composite with manganese dioxide to give improved electrochemical performance (Table 1.4).

1.3 Objectives

Nanostructured MnO_2 adopts various crystallographic forms depending upon the size of the tunnel resulting in distinct physical and chemical characteristics with their variety of applications in catalysts, sensors, electrodes for electrochemical batteries, and supercapacitors. Due to their potential applications, MnO_2 have received a lot of attention in research communities. In order to achieve a stable structure, tunnels and interlayers spacing present in α-, β- and δ-MnO_2 acquire supplementary metal ions, water molecules or vacancies. In this context, MnO_2 displays a variety of magnetic ordering in different phases with varying electrochemical performance whose behaviour is still not well understood.

Researchers have shown that the structural and molecular modifications can be used to study magnetic and electrochemical properties of the polymorphs of MnO_2. As a result, the synthesis and study of the properties of MnO_2 structures with various morphologies are critical for a variety of applications. Researchers have shown tuned structural and magnetic properties with electrochemical performance of MnO_2 after incorporating dopants within the tunnels. However, RE doped MnO_2 has not been studied either from magnetic point of view or on the basis of its electrochemical performance. Therefore, it is of interest to study regression of structural and magnetic characteristics with electrochemical performance of MnO_2 after the incorporation of Dy ion. Detailed study of the polymorphs (α, β, δ and mixed phase of α and β) of MnO_2 and Dy doped MnO_2 are included in the thesis as the following chapters:

- Chapter 1 accounts for the introduction and review of the literatures on the topics that been studied in this work. In chapter 2, we have studied the synthesis and experimental techniques adopted to synthesize and characterize the materials.
- In chapter 3, we synthesise α, β, and mixed phase of α and β-MnO_2 using hydrothermal technique. Further, the structural and microstructural analysis has been done employing XRD, FT-IR, FE-SEM and XPS. In this chapter we examine thorough research on the magnetic characteristics, including the understanding of magnetic and SG like ordering based on varying concentrations of Mn^{3+}/Mn^{4+} in all sample.
- In chapter 4, we discuss the synthesis of δ-MnO_2 and study its structure, microstructure through XRD and Raman spectroscopy. The surface morphology and oxygen vacancies are determined through FE-SEM, TEM and XPS. The magnetic properties are

evaluated from magnetization versus temperature, magnetization versus field, remanent magnetization and frequency dependent ac susceptibility measurements.

- In chapter 5, we examine the effect of doping Dy ion on electrochemical performance of α-MnO_2 nanorods synthesised using simple and facile hydrothermal method. (5 mol % of Dy doped α-MnO_2 electrode accelerates mass transport, improve the electrode kinetics investigated extensively employing cyclic voltammetry (CV), Galvanostatic charge/discharge (GCD) and electrochemical impedance spectroscopy (EIS). The structural, morphological and surface area analysis has been performed using X-ray diffraction, Raman spectroscopy and BET and BJH method. The influence of doping Dy in α-MnO_2 nanorods on its specific capacitance has been explained in this chapter.
- In chapter 6, we illustrate the evolution in magnetic characteristics after doping Dy in α-MnO_2 nanorods made by one step hydrothermal method. Magnetic properties are evaluated using magnetization versus temperature and magnetic field versus temperature measurements. Furthermore, we quantify the exchange bias and training effect, which are discussed in terms of various phenomenological models.
- Finally, chapter 7 has been committed to sum up of the major findings of the thesis. By the end, the future scope of the work related to the present thesis has been briefly outlined.